Accepted Manuscript

Precision Engineering

Title: Mechatronic design, actuator optimization, and control of a long stroke linear nano-positioner

Authors: Ahmet Okyay, Kaan Erkorkmaz, Mir Behrad Khamesee

Please cite this article as: Okyay Ahmet, Erkorkmaz Kaan, Khamesee Mir Behrad.Mechatronic design, actuator optimization, and control of a long stroke linear nano-positioner.*Precision Engineering* https://doi.org/10.1016/j.precisioneng.2018.01.007

This is a PDF file of an unedited manuscript that has been accepted for publication. As a service to our customers we are providing this early version of the manuscript. The manuscript will undergo copyediting, typesetting, and review of the resulting proof before it is published in its final form. Please note that during the production process errors may be discovered which could affect the content, and all legal disclaimers that apply to the journal pertain.

Mechatronic design, actuator optimization, and control of a long stroke linear nano-positioner

(Abbr: Mechatronic design of nano-positioner)

Ahmet Okyay, Kaan Erkorkmaz*, Mir Behrad Khamesee

University of Waterloo, 200 University Ave. West, N2L3G1, Waterloo, ON, Canada

*Corresponding author: Tel: +1-888-519-4567 ext. 35214, Fax: +1-519-885-5862
E-mail address: kaane@uwaterloo.ca

Highlights
- A novel mechatronic design, based on complementary voice coil actuators (VCA's) to improve force linearity, and co-use of an air bushing pair with a single flat air bearing, to achieve a simple, low-cost, and self-aligning structure.
- Experimental achievement of +/-5 nm positioning resolution over a stroke of 20 mm with a nominal positioning cross-over frequency of 450 Hz.
- Topology based optimization of VCA pair magnetic properties to maximize acceleration and minimize thermal losses.
- High-order modeling of VCA's electrical dynamics, including effect of Eddy current losses.
- Controller design via loop shaping and harmonic error correction in the encoder feedback.
- Prediction and experimental validation of the stage's performance via Dynamic Error Budgeting (DEB).

Abstract:
In this paper, mechatronic design, actuator optimization and controls of a long-stroke (20 mm) linear nano-positioner are presented. The mechatronic design is described in terms of the stage's most prominent features regarding mechanical design, assembly, actuator configuration, and power supply. A novel air-bearing/bushing arrangement has been used in which the commonly employed double shaft arrangement is replaced with a single shaft supported by an air bearing from the bottom to constrain the roll motion. The assembly is greatly simplified by exploiting the self-aligning property of the air-bushings which are held in the housings by O-rings. Also, the footprint of the stage is reduced. Voice coil actuators (VCA) in moving magnet mode have been used in complementary double configuration for uniformity of force response. The performance objectives of previously optimized VCA's as standalone actuators are re-evaluated in this configuration. It is observed that while the performance objectives decrease a bit, the desirability of the design point is still retained. Controller design has been made for the current control and position control loops. Heydemann's method for the compensation of encoder quadrature detection errors is implemented. The positioning resolution of the stage as measured from the sensor output is experimentally determined to be +/-5 nm. Dynamic Error Budgeting (DEB) method has been used to analyze the contributing factors to the positioning error, and sensor broadband noise is determined to be the major contributor. The actual positioning accuracy of the stage is estimated by DEB to be 0.682 nm root-mean-square (RMS). The trajectory following accuracy is determined to be +/-

15 nm. It is expected that trajectory following accuracy can substantially improve if more advanced compensation methods for encoder quadrature errors are implemented.

Keywords:

Voice coil actuator, topology optimization, Dynamic Error Budgeting, air bearing, nano-positioning, optical encoder, encoder quadrature detection errors, eddy currents

1. Introduction

Precision motion systems find a broad range of application in micro/nano machining tools, lithography scanners, testing and metrology machines, micro-assembly, biotechnology, optics manufacturing, magnetic data-storage, optical disk drives, and so on [1-3]. Various technologies for the actuation, bearing system, and position sensing of such systems have been employed depending on the desired number of motion axes, motion range, and positioning resolution.

The number of motion axes among ultraprecision motion stages range from single - axis / linear to 6 degrees of freedom (DOF). The number of motion axes has a profound effect on the choice of bearing technology. As expected, most 6 - DOF stages [4-7] employ magnetic levitation (maglev) to avoid bearing contact. One shortcoming of this method is the necessity to constantly power the coils which provide the levitation force. Alternatively, Shamoto et al. [8] have proposed a 6-DOF stage using a 'walking drive', in which nine pairs of piezoelectric actuators provide actuation in all 6 axes through a series of strokes. In the case of $XY\theta$ stages (i.e., planar stages with rotation capability), the stages can be supported from the bottom with air bearings [9-11] or flexures [12, 13]. Both air bearings and flexures are virtually free from friction and provide theoretically infinite motion resolution. Air bearings typically have lower bearing stiffness and require tight tolerances in the manufacturing of the mating components. On the other hand, flexures require actuators to be powered during position holding. Also, they need to be proportionally larger for higher stroke lengths to limit their stiffness.

Among different actuator alternatives, voice coil actuators (VCA) based on Lorentz forces have been researched extensively [4, 5, 9, 10, 14-17], possibly due to their non-contact, continuous operation which is free from hysteresis, force/torque ripple, and backlash [18, 19]. In stages supported by magnetic levitation [4, 5], VCA's are used for both bearing forces and maneuvering. In some other cases, linear motors employing Halbach magnet arrays are used to generate actuation and levitation forces at the same time [6, 7, 20]. In [6], stator windings with different orientations are overlaid on top of each other in a compact printed circuit board (PCB) structure, making the design more feasible for large motion ranges. The PCB stator was also employed in [7] for a 6 DOF rotary table. In [21] a rotary VCA is combined with a translational tubular VCA in a single shaft design supported by air bushings, to achieve rotary-linear motion. A close alternative to VCA is the usage of reluctance actuators [12] which provide higher force density, maximum forces, and power efficiency. The inherent nonlinearity in such systems can sometimes be remedied using a special design to linearize the response, as [22] proposed for a fast tool servo (FTS).

2

Numerous single axis ultraprecision stages have also been proposed [14, 15, 17, 23-29]. Using VCA's with optical encoders [14, 15, 17], several millimeters of motion range with nanometer level resolution could be achieved. For smaller motion ranges less than 0.5 mm, capacitance sensors could be used [24, 29]. Stacked designs combining multiple actuation and bearing technologies have also been proposed [25-27], where the fine positioning resolution is preserved over extended motion ranges (>50 mm).

In this paper, mechatronic design, actuator optimization, and control of a long stroke (20 mm) linear nano-positioner is presented. The nano-positioner employs a novel air-bushing/bearing arrangement in which the moving body consists of plates attached to a single shaft engaging to air bushings. Instead of the commonly utilized double shaft arrangement, the roll resistance is provided by an air bearing placed underneath the moving body. This way, the self-aligning property of the air bushings which are held in the housings by O-rings is exploited to a high degree, the assembly is greatly simplified, and the footprint of the stage is reduced. The nano-positioner is actuated by voice coil actuators (VCA) in complementary double configuration for uniformity of force response along the stroke length. In our earlier research, performance of a single standalone VCA was optimized based on the acceleration per current density and the motor constant, which is a measure of force produced per power dissipated [30]. In this paper, performance optimality for the application of two VCA's arranged in a complementary double configuration is verified. The nano-positioner can achieve +/- 5 nm positioning accuracy, and +/- 15 nm trajectory following accuracy. The positioning accuracy is analyzed using the Dynamic Error Budgeting (DEB) method, and the contributions of various disturbances to the positioning error are determined.

This paper is organized as follows: The mechatronic design is detailed in Section 2 with emphasis on the most prominent design features. A brief summary of VCA design and the re-calculation of performance objectives for the complementary double configuration are presented in Section 3. System identification and controller design for the current and position control loops, including the analysis of eddy current effects, experimental verification of the positioning and trajectory following accuracies, as well as DEB analysis of the positioning resolution are presented in Section 4. The concluding remarks are provided in Section 5.

2. Mechatronic design
In this section, first a conceptual design of a low-cost desktop micro-milling machine is presented, which places the nano-positioner in context in terms of design goals. Following that, a list and explanations of the most prominent design features of the nano-positioner are presented.

2.1. Conceptual design for a low-cost desktop micro-milling machine
Front and back views for the conceptual design of a low-cost desktop micro-milling machine are presented in Fig. 1. The proposed design utilizes air bushings/bearings for high positioning resolution. Voice coil actuators working in moving magnet mode are preferred for non-contact and continuous actuation. With the design, workpiece dimensions of 20 mm x 20 mm x 20 mm are targeted. Servo accuracy is intended to be in the order of nanometers, and part accuracy to be a few microns. A pneumatic counter-balance is built-in to cancel out the effect of gravity; hence, running a constant

3

current on the vertically oriented actuator is avoided. This way, excessive heating of actuator coils is prevented. The linear nano-positioner described in this paper corresponds to a prototype version of the X positioning axis of the micro-milling machine. Its design is further detailed in the following.

2.2. Mechatronic design of the nano-positioner

The exploded view and photograph of the long-stroke linear nano-positioner is presented in Fig. 2. The most prominent design features of the stage can be outlined as follows:

i.   An air-bearing/bushing arrangement has been used in which the commonly employed double shaft arrangement (like the ones used in the Y and Z motion axes of the micro-milling machine in Fig. 1) is replaced by a single shaft supported by an air bearing from the bottom to constrain the roll motion. This way, manufacturing and assembly are greatly simplified by exploiting the self-aligning property of the air-bushings, which are held in the housings by O-rings. The necessity of complex fabrication procedures and specialized fixtures is eliminated. Also, the footprint of the stage is roughly reduced by half, which is important for suitability in desktop applications and in multiple arrangements in a work center. After the guideways are self-aligned, under pneumatic pressure, an epoxy material can be injected into the cavity between the air bushings and the housings to achieve further stiffness in the radial direction [31, 32].

ii. VCA's are used in moving magnet (MM) mode. Although this increases the overall moving mass, it is considered a good trade-off from the moving coil configuration, by eliminating possible parasitic forces due to lead cables. Such forces degrade both the positioning accuracy under no-load conditions and the repeatability, by acting as an uncertain disturbance force. VCA's have been preferred over linear motors due to the small motion range required in this application, as well as their ripple-free, continuous force output. Also, in contrast to the linear motors which require a three-phase power source and a more complicated current controller design, VCA's have been powered using single-phase, linear amplifiers.

iii. The complementary double VCA configuration has been used to provide near uniform force response per supply current over the whole stroke. Actuator force factor (K_f) is simulated using COMSOL® finite element analysis (FEA) as shown in Fig. 3. It is observed that the combined force response is mostly uniform, allowing better linearization of the overall positioning system, and higher bandwidth control to be achieved without compromising stability margins or requiring explicit gain scheduling.

iv. The shaft, top and bottom plates are made of Aluminum 6061 for reduced mass, corrosion resistance, and the prevention of electromagnetic attraction. Support structures are also made of the same material. The shaft is precision ground to achieve the tight tolerances (g6) and the surface quality (Rq16) required by the air bushings [31,33].

v.   To minimize unwanted moment generation during actuation, the top and bottom plates are sized to align the axis of actuation with the center of mass, using CAD program calculations.

vi. The discharge of compressed air from the air bushings and bearings helps to remove heat which is mainly produced by the actuator coils, by acting like a heat sink. Although the convective coefficient of heat transfer is relatively high in the air-bushing / shaft interface, due to the

4

limited mass flow rate, the heat removal is only partially effective in isolating the payload from thermal disturbances.

vii.   VCA cores are mounted at the two ends of the shaft using the method detailed in Fig. 4 to prevent variations due to screw thread. The mating extension of the shaft and the hole on the VCA core are prescribed tolerances such that their centers are aligned within 17.5 μm. The mating extension and hole can be applied a taper to further improve the alignment.

viii.   Linear current amplifiers are preferred over PWM amplifiers to power the VCA coils due to better noise characteristics [34]. Due to the relatively low power requirements of the stage, lower efficiency and heating problems of linear amplifiers are considered manageable in the case of miniature-range actuators. Linear Current Amplifier Module (LCAM) from Quanser® [35] has been used. The current controller is implemented by tuning the op-amp circuit with passive electronic components derived from the required controller parameters.

The specifications of the computer control system and the position sensor are detailed in Section 4.2.

3. Actuators

Schematic drawing of the VCA's is presented in Fig. 5. Values of the design variables are presented in Table 1. The VCA design was previously optimized in [30] considering the response of a single VCA when the coil is fully engaged to the magnetic core. Performance topologies of the optimization objectives were plotted with respect to $\{r_1, p\}$. The rest of the variables were set according to the scale of the required forces, stroke length, manufacturing/assembly tolerances, etc. In this section, the optimization objectives are modified according to the complementary double configuration, and the performance topologies are re-calculated and verified.

When the VCA core and the coil are fully engaged, the force response can be approximated as,

$$F = S V_c B_{gap} J \,,$$

1)

where, $0 < S < 1$ is the coil packing efficiency of winding, V_c is the coil volume, B_{gap} is the magnetic flux density at the middle of the gap, and J is the current density. The optimization objectives, acceleration per current density (σ_{acc}), and the motor constant (K_M) are derived as:

$$\sigma_{acc} = \frac{S V_c B_{gap}}{m_{eq}} \,,$$

2)

$$K_M = \frac{F}{\sqrt{Q}} = \sqrt{\frac{S V_c B_{gap}^2}{\rho}} \,,$$

where m_{eq} is the equivalent mass per VCA, Q is the heat dissipation per VCA, and ρ is the resistivity of copper. The equivalent mass is expressed as,

5

$$m_{eq} = m_{tot} / n \, ,$$
$$= m_{stage} / n + m_{core} .$$

Above, m_{tot} is the total mass, n is the number of VCA's, m_{stage} is the mass of the motion stage without the VCA cores attached, and m_{core} is the mass of each VCA steel core. In this formulation, as carried out in the earlier analysis [30], multiple VCA's are assumed to operate in parallel, i.e. at the same fully engaged condition. Maximizing acceleration per current density (σ_{acc}) and the motor constant (K_M) maximizes the stage acceleration capacity and the force produced per heat generation, respectively.

In the complementary double VCA case, due to the special arrangement of the actuators, while the core of one VCA is engaging into the coil, the other is disengaging. Referring to Fig. 3, at the $x = 0$ mm position, while the left VCA is responding with the force F_{100} (100% engaged), the right VCA is responding with F_0, producing a total of $F = F_{100} + F_0$. Even at the fully disengaged case, the VCA can still produce forces due to the interaction of the coil current with the flux leaking outward the core. The same interaction is observed for the disengaged portion of the coil at the partially engaged position. Hence, $F_0 > 0$ and $F_i + F_{100-i} > F_{100}$. In the proceeding analysis, the mean total force response (F_m) has been calculated from the total responses at $x = 0, 5, 10, 15, 20$ mm as,

$$F_m = \frac{(F_0 + F_{100}) + (F_{25} + F_{75}) + (2F_{50})}{3} . \tag{4.1}$$

The optimization objectives have been modified to take into account the mean total force response as,

$$\sigma'_{acc} = \frac{F_m}{m_{tot} J} ,$$

$$K'_M = \frac{F_m}{\sqrt{2Q}} . \tag{4.1}$$

Performance topologies calculated for the modified optimization objectives are presented in Fig. 6. It is observed that the design point still constitutes an acceptable compromise between the maximum locations of the two optimization objectives. Performance objectives are evaluated at the design point { r_1 = 7.5 mm, p = 0.2 mm} as, σ'_{acc} = 1.48 ($N \cdot mm^2 \cdot kg^{-1} \cdot A^{-1}$), and K'_M = 3.27 (N/$\sqrt{W}$). The values are 35% and 8% lower than the former formulations with the fully engaged case [30], respectively. This is due to the fact that two VCA's in the complementary double configuration perform less than two VCA's fully engaged and operating in parallel, but they yield much better force uniformity, as mentioned

6

in Section 2.2. It is inevitable for the current design that the coil and the core disengage proportional to the motion stroke. The design point still constitutes a good compromise between maximum acceleration per current density (σ'_{acc}) and maximum force per heat dissipation (K'_M) through the choice of r_1 = 7.5 mm around the mid-point, while the choice of p = 0.2 mm enables better aligned flux lines.

4. Control system

The overview of the position control loop is presented in Fig. 7. It is composed of the position controller ($C(s)$) and the overall plant ($G_p(s)$). The overall plant is made up of the current control system (K_a), VCA force response (K_f), stage free body dynamics, and possible additional dynamics due to vibration modes and parasitic forces ($G^*(s)$).

A more detailed version of the control system block diagram, showing particulars of the current control loop, VCA force response, and the encoder correction, is presented in Fig. 8. Two independent current control loops are implemented for VCA's 1 and 2 (left and right). For actuator 2, the current command is multiplied by -1 to accommodate the reversal of the force direction with respect to the sign of the current. Individual force factors of the two VCA's are expressed by K_{f1} and K_{f2}, which are combined in the overall plant model ($K_f = K_{f1} + K_{f2}$) once the two current loops are designed to have nearly identical dynamics. An 'encoder correction' block in the feedback path is also shown, which represents the compensation of encoder measurement errors as detailed in Section 4.4.1.

4.1. Current control loop

In this section, VCA electrical dynamics is investigated and the current controller is designed.

4.1.1. VCA electrical dynamics

VCA electrical dynamics is indicated in Fig. 8 by the commonly assumed first-order transfer function,

$$G_m(s) = \frac{K_m}{\tau s + 1}$$

(4)

where $K_m = 1/R$ is the DC gain, and $\tau = L/R$ is the time constant. The resistance of the VCA coil is given as $R = 3.57\ \Omega$. Coil inductance at 100% and 0% engagement levels are computed by FEA as, L_{100} = 25.6 mH and L_0 = 5.2 mH, respectively. In order to verify this model, current frequency response to voltage excitation of the VCA's were measured as shown in Fig. 9.

The measurement was carried out for both VCA's in both the fully-engaged (100%) and the fully-disengaged (0%) positions. The frequency response function (FRF) is also simulated using COMSOL® FEA. Experimentally measured and FEA simulated responses are observed to be close. The frequency response predicted by the first-order resistance + inductance (LR) model is also plotted. It is observed to

deviate significantly from the measured and simulated responses. In order to clarify the nature of the deviation, FEA simulated FRF's are fitted a transfer function (TF) using Matlab® function 'lsqnonlin' in the Optimization Toolbox [36] of the form,

$$G_m(s) = \frac{K(s+z_1)(s+z_1)}{(s+p_1)(s+p_2)(s+p_3)}.$$

5)

Above, $z_{1,2}$ are zeros, $p_{1,2,3}$ are poles, and K is the gain, values of which are presented in Table 2, alongside the predicted pole from the LR model ($1/\tau$). The first pole of the fitted TF is observed to be close to the prediction by LR. At higher frequencies, the response deviates from the LR prediction due to the additional poles and zeros. The resulting mismatch in phase becoming most evident at around 1000 Hz is especially critical for controller stability, as it corresponds to the desired current control bandwidth. The screenshot from the FEA software (Fig. 10) reveals that the additional dynamics is due to the eddy currents induced in the stator structure, mainly the mandrel and the coil bracket. This is further verified by the fact that when the conductivities of iron and Aluminum are set to zero, FEA results become identical to LR – model predictions, as shown in Fig. 9.

4.1.2. Design of the current controller

The current controller comprises an integrator and a lead filter, given by,

$$C_c(s) = K_c \frac{1}{s} \frac{T_c s + 1}{\alpha_c T_c s + 1}, \ 0 < \alpha_c < 1,$$

5)

The same controller structure is used for both VCA's. Controller parameters (K_c, T_c, α_c) are implemented by the selection of passive electronic components in the analog controller circuit with op-amps. The current controller is designed taking the loop-shaping approach [37, 38]. The controller (C_c) and loop ($L_c = C_c G_m$) transfer functions are plotted in Fig. 11. A minimum crossover frequency of ω_c = 1000 Hz and a minimum phase margin of PM = 40° is targeted. The common practice in loop-shaping controller design is to place the peak phase contribution of the lead filter at the desired cross-over frequency. However, due to the VCA's inherent recovery of phase around 1000 Hz, a lead filter with a maximum 63° phase contribution at 122 Hz has been implemented such that the resulting closed loop transfer functions are flat at low frequencies and have a reasonable peak around the cross-over frequency. Cross-over frequencies and phase margins for each case are summarized in Table 3.

The closed-loop transfer function (CLTF) has been measured using frequency response for different levels of engagement, as presented in Fig. 12. The effect of transport delay due to the sampling frequency, F_s = 20 kHz of the analog-to-digital converter (ADC) has been compensated by adding ϕ =

$\left(360 \times \dfrac{f}{F_s}\right)^{\circ}$ to the measured phase at each frequency point (f). This estimate is based on the

8

observation that the delay corresponded to one complete sample. For the 100% and 0% cases, predicted CLTF using the measured $G_m(s)$ and the current controller TF have also been overlaid. Best (highest) and worst (lowest) current control bandwidths (BW) as measured are summarized in Table 4.

4.2. Position control loop

The position controller has a lead/lag structure given by,

$$C(s) = K_p \frac{T_a s + 1}{\alpha_a T_a s + 1} \frac{T_d s + 1}{\alpha_d T_d s + 1}, \ 0 < \alpha_a < 1, \ \alpha_d > 1.$$

)

The variables of lead (α_a, T_a) and lag (α_d, T_d) filters are determined using the loop-shaping controller design methodology, similar to the current control loop. Prior to the controller design, the frequency response of the overall plant ($G_p(s)$) is measured at the x = 10 mm position as presented in Fig. 13a. As can be seen, up to about 500 Hz, double integrator-like dynamics are dominant. At higher frequencies, the phase is expectedly rolling-off due to the closed loop current control phase loss.

The controller ($C(s)$) Bode plot is presented in Fig. 13c up to the Nyquist frequency of 10 kHz for both continuous and the discretized versions using Tustin transformation. Positioning loop TF ($L(s)$) magnitude and Nyquist plots are presented in Fig. 13b. A cross-over frequency (ω_c) of 450 Hz has been achieved, along with a phase margin (PM) of 40° and a gain margin (GM) of 1.96. The lag filter is implemented with α_d = 100, and the zero ($1/T_d$) is placed at ω_c/10. The lead filter is designed to recover 74° phase at the cross-over frequency, hence achieve the desired PM. The position controller design has been carried out in conjunction with the modal testing results of the nano-positioner [39]. The lowest vibration mode has been identified to be a roll-mode at 65 Hz natural frequency. However, this mode is not observed to interfere with the position control, hence not affect the stability.

Although it is common practice to set the position control bandwidth at least a decade away from the current control bandwidth (about 1 kHz) where it has a constant gain, stability could still be guaranteed at ω_c = 450 Hz, with adequate phase and gain margins, using the experimentally measured frequency response function for $G_p(s)$ (Fig. 13a). Stability analyses using the reconstructed L from the varying closed loop current responses (K_a) and force responses (K_f) along the positions x = 0, 5, 10, 15, 20 mm of the VCA's, as well as the mass of the stage ($1/ms^2$), indicated the cross-over frequency to vary between 418 – 492 Hz, and the phase margin to vary between 47° – 57°. Hence, stability is assured within similar bounds along the whole motion stroke of the stage, regardless of the changes in the VCA engagement, particularly due to the uniformity of the force response in the complementary double configuration (Fig. 3).

The digital position controller is implemented on the DSpace® DS1005 control system sampling at 20 kHz. The controller transfer function is discretized using Tustin's method, which results in closely

9

matching frequency response characteristics. The encoder scale (Heidenhain® LIP501 R) has 8 µm grating period. The encoder reading head with integrated interpolation (Heidenhain® LIP58) outputs two 90° phased measurement signals A and B with 4 µm period [40].The encoder signal is connected to the DSpace® DS3002 encoder interface which allows 4096 times interpolation using arctangent formulation, hence achieving 0.97 nm measurement resolution. The voltage commanded to the amplifiers by the controller is transmitted via a DSpace® DS2102 digital-to-analog converter (DAC) with ±10 V range and 16-bit resolution, corresponding to a least significant bit (LSB) of 0.305 mV. An analog-to-digital converter (ADC) DSpace® DS2001 is used to gather fault and current measurement signals from the amplifier boards. The ADC has the same range and resolution specifications as the DAC. It is also used to measure encoder A and B signals separately to initialize the encoder signal correction scheme described in Section 4.4.1.

4.3. Positioning resolution analysis via Dynamic Error Budgeting

In this section, the positioning resolution of the nano-positioner is experimentally measured using a step trajectory. Then, Dynamic Error Budgeting (DEB) [41] method is used to analyze the positioning performance.

4.3.1. Positioning results

Positioning performance is measured using a reference trajectory obtained by smoothing a step trajectory composed of 200 nm increments, using a second-order filter at 40 Hz with a damping ratio of ζ = 0.8. The results obtained using this trajectory is presented in Fig. 14. No filtering was applied on the encoder measurements in this or any of the results presented in this paper. Closed loop positioning resolution is observed to be ±5 nm, compared to the 0.97 nm peak-to-valley resolution of the encoder signal.

4.3.2. DEB calculations

The block diagram of the position control system with the plant input level disturbance (d) and the position measurement noise (v) signals indicated is presented in Fig. 15. In the figure, x_{ref} (generally denoted as r) is the positioning reference input, e is the control error, u is the control effort, x is the actual position, and $\tilde{x}$ is the measured position. To differentiate between the control error ($e = x_{ref} - \tilde{x}$) and the actual error of positioning, the actual error of positioning can be denoted as $a = x_{ref} - x$.

Relating to feedback control theory [38], the sensitivity (G_S), complementary sensitivity (G_T), and input disturbance response (G_D) transfer functions are given by:

$$G_S = \frac{1}{1 + CG_p}, \ G_T = \frac{CG_p}{1 + CG_p}, \ G_D = G_S G_p.$$
(3)

The control error and the actual error can be expressed as:

10

$$e = G_S\, r - G_D d - G_S v \ ,$$
$$a = G_S\, r - G_D d + G_T v \ .$$

)

Bode plots of G_S, G_T, and G_D are shown in Fig. 16, based on controller and plant models established in Section 4.2. Using linear time-invariant system theory and assuming that the signals are uncorrelated [42], Eqn. (9) can be written in terms of power spectral densities (PSD) as,

$$S_e(f) = |G_S|^2\, S_r(f) + |G_D|^2\, S_d(f) + |G_S|^2\, S_v(f),$$
$$S_a(f) = |G_S|^2\, S_r(f) + |G_D|^2\, S_d(f) + |G_T|^2\, S_v(f).$$

)

Above, $S_e(f), S_a(f), S_r(f), S_d(f), S_v(f)$, are one-sided power spectral density distributions of e, a, r, d, v, respectively, vs. frequency (f). Other definitions pertaining to the proceeding application of DEB are presented in Table 5.

PSD's of the signals (r, d, v) are obtained as follows:

- $S_r(f)$ is obtained from the time domain step trajectory reference signal.
- $S_d(f)$ is associated with the quantization noise of the DAC which transmits the control command to the amplifiers. Using the LSB of δ_{dac}= 0.305 mV and since the quantization noise can be characterized as a uniform distribution between $-\delta_{dac}\ldots+\delta_{dac}$ [43], it can be obtained as:

$$\sigma_{dac}^2 = \frac{\delta_{dac}^2}{12} = 7.8 \text{ x } 10^{-9}\ (V^2),$$

L)

$$S_d(f) = \frac{\sigma_{dac}^2}{f_N} = 7.8 \text{ x } 10^{-13}\ (V^2/Hz),\ 0 < f < 10 \text{ kHz}.$$

- For the determination of the encoder measurement signal noise PSD ($S_v(f)$), the encoder signal is measured at a static position as shown in Fig. 17a. Then, the DFT is calculated which has a low frequency component due to drift and a high-frequency broadband component as shown in Fig. 17b. The resulting CPS has a 8.54 (nm^2) component at 0 Hz due to the drift, and a straight line shape with small irregularities at high frequency. The PSD associated with the broadband component is calculated from the slope of the CPS at high frequencies, as shown in Fig. 17c. Using the slope of CPS allows for the average value of broadband encoder noise to be visualized and estimated in a somewhat clearer and meaningful way than directly working with the PSD or DFT. Hence, this component has been estimated and modeled as white noise, given by,

11

$$S_v(f) = 1.9 \times 10^{-4} \text{ (nm}^2\text{/Hz)}, \ 0 < f < 10 \text{ kHz.}$$

The cumulative power spectra (CPS_r, CPS_d, CPS_v) contributed by each signal are calculated based on the PSD models and the transmission TF's (G_S, G_T, G_D), e.g. $CPS_{e,v}(f_k) = \sum_{i=1}^{k}|G_S|^2 S_v \, df$ for the contribution of v in e.

4.3.3. DEB results and discussion

In the DEB approach, contribution of different signals on the performance objectives, which are the signals e and a, are presented in terms of their CPS. As the last element of the CPS in the frequency spectrum equals the variance of the signal, this kind of presentation allows for a comparison of the impact of different disturbances and the observation of the build-up of errors through different frequency ranges due to the system dynamics.

The first set of DEB results are obtained for the control error (e) as shown in Fig. 18. These results mainly serve the purpose of verifying the PSD models of the disturbances. CPS_e^* is obtained from the actual time domain e signal. CPS_e is constituted from the estimated individual contributions of r, d, v, through system transfer functions identified in Section 4.3.2, according to Eqn. (9) . The estimated error variance (σ_e^2) differs by only 4.7% from the measured error variance ($\left(\sigma_e^*\right)^2$). This shows that the disturbance models are adequate for an overall assessment of the controller design. Evaluation of the individual CPS contributions shows that higher frequencies are dominated by the broadband measurement noise originating from the sensor ($CPS_{e,v}$). Lower frequencies are dominated by the requirement to follow the smoothened step trajectory ($CPS_{e,r}$). A negligible component also exists due to the DAC quantization noise ($CPS_{e,d}$). The small $CPS_{e,d}$ builds up at the lower frequency region and saturates around 1000 Hz due to the attenuation of the respective TF (G_D).

The actual positioning error (a) can be predicted from the same signal PSD and transmission models as shown in Fig. 19. The RMS of the actual positioning error can be calculated as σ_a = 0.682 nm. Contrary to the control error, CPS contribution to the actual positioning error from the encoder measurement noise ($CPS_{a,v}$) saturates at around 2000 Hz due to the attenuation of G_T, unlike G_S. This is the major reason why the estimated value of the actual error (a) is much better than that of the control error (e).

From the examination of Fig. 19, it can be concluded that the control bandwidth has to be lowered in order to shift G_T to the left and reduce the contribution of measurement noise in the positioning error.

12

However, as this would also shift G_S to the left, it would increase the contribution from the trajectory tracking error ($CPS_{a,r}$). In the case of the filtered step trajectory, this would seem acceptable, however, for the wider range of faster and rapidly changing trajectories, for which the nano-positioner is intended, it would result in poor positioning results. In addition to lifting $CPS_{a,v}$ up, increasing the bandwidth would also increase the control effort ($u=Ce$), by admitting more of the measurement noise. a practical trade-off between command tracking and disturbance rejection versus measurement noise permeation, the control cross-over frequency is chosen as 450 Hz. A static error budget of the system has also been conducted using laser interferometric metrology and modelled thermal disturbances [39].

4.4. Trajectory following performance
While following a trajectory with high feedrate, periodic measurement errors due to encoder quadrature detection generate high frequency harmonic signal components, which are highly detrimental to the control system. In this section, first, a compensation scheme for these measurement errors are implemented, and then the improvement in the trajectory following performance of the nano-positioner is experimentally validated.

4.4.1 Compensation scheme for encoder quadrature detection errors
The linear encoder system ideally outputs two 90° phased sinusoidal signals (A and B) with 4 μm period as follows:

$$A = M \cdot \cos(\varphi),$$
$$B = M \cdot \sin(\varphi),$$
$$\varphi = \left(\frac{2\pi}{\lambda}\right) \cdot x \bmod \lambda + \varphi_o.$$

(3)

Above, M is the amplitude of the signal, φ is the angular measurement of displacement, λ = 4 μm is the signal spatial period, and φ_o is the angle when encoder was reset ($x \to 0$). Heydemann [44] had proposed a mathematical model for the distorted A and B signals which originate from the mechanical misalignment of the encoder reading head to the encoder scale as well as electrical signal imbalance, as follows:

$$A' = a \cos(\varphi) + A_o,$$
$$B' = b \sin(\varphi - \theta) + B_o.$$

(4)

In Eqn. (14), a, b are distorted signal amplitudes, θ is the phase error, and A_o, B_o are the offsets. The parameters of the signal distortion model as presented in Table 6 have been identified by least-squares fitting to the data points obtained through the whole motion range of the nano-positioner. Using the

13

signal distortion model, a compensator has been implemented which subtracts the calculated measurement error from the encoder output, as was shown in the block diagram of Fig. 8.

4.4.2. Cubic acceleration profile trajectory test

The trajectory following performance has been tested with a jerk limited cubic acceleration profile trajectory with maximum feedrate, acceleration, and jerk values of F = 3 mm/s, A = 3 mm/s^2, J = 12 mm/s^3, respectively, as shown in Fig. 20. The tracking results in Fig. 21 show that the control error is confined to the +/- 45 nm range when the compensation for measurement errors is turned off, and shrinks down to +/- 15 nm with the help of compensation. Similarly, control effort signal is reduced by half from +/- 0.1 V to +/- 0.05 V. DFT of the control error during constant feedrate motion (2.5 - 4.5 s) is presented in Fig. 22. As expected, errors are clustered around the periodic error (3 (mm/s) / 4 μm = 750 Hz) and its harmonics at 1500, 2250, 3000 Hz. Values of DFT at each harmonic are presented in Table 7. It is observed that the compensation method has reduced the first two harmonics (750 Hz, 1500 Hz) more than 8-fold. On the other hand, it had little effect on the third harmonic (2250 Hz), and has slightly worsened the forth harmonic (3000 Hz). As Heydemann's model (Eqn. (14)) allows for the elimination of φ from the least-squares formulation, it was chosen as a practical compensation method during the validation of the controller. Future research will also focus on multi-harmonic compensation methods, in order to further mitigate the dynamic servo errors.

5. Conclusion

The long-stroke linear nano-positioner designed in this paper utilizes a novel air-bushing/bearing arrangement for simplified assembly and reduced footprint. The suitability of the complementary double VCA configuration is validated by recalculating the optimization objectives. Eddy current effects on the measured VCA dynamics is confirmed via simulations. The stage has been verified to be able to deliver a positioning resolution of 5 nm within 20 mm motion range, corresponding to a dynamic range of 4 million. Using the Dynamic Error Budgeting method, the stage's actual positioning accuracy has been estimated to be 0.682 nm RMS. The compensation method by [44] for encoder quadrature detection errors is observed to work reasonably well for the verification of the trajectory following performance. On the other hand, a better compensation method can be used in the future to suppress more harmonics caused by the measurement error.

References

[1] Bishop RH, ed. The Mechatronics Handbook, 2 Volume Set. [e-book] CRC Press, 2002.

[2] Schmidt RM, Schitter G, Rankers A. The Design of High Performance Mechatronics, High-Tech Functionality by Multidisciplinary System Integration. Amsterdam: IOS Press, 2014

[3] Tan KK, Lee TH, Huang S. Precision Motion Control: Design and Implementation, 2nd ed. [e-book] Springer, 2008.

[4] Kim WJ, Verma S, Shakir H. Design and precision construction of novel magnetic-levitation-based multi-axis nanoscale positioning systems. Prec Eng 2007; 31; 337-50

[5] Zhang Z, Menq C-H. Six-axis magnetic levitation and motion control. IEEE T Robot 2007; 23; 196-205

[6] Lu X, Usman I. 6d direct-drive technology for planar motion stages. CIRP Ann-Manuf Techn 2012; 61; 359-62

[7] Lu X, Dyck M, Altintas Y. Magnetically levitated six degree of freedom rotary table. CIRP Ann-Manuf Techn 2015; 64; 353-56

[8] Shamoto E, Murase H, Moriwaki T. Ultraprecision 6-axis table driven by means of walking drive. CIRP Ann-Manuf Techn 2000; 49; 299-302

[9] Choi Y-M, Kim JJ, Kim J, Gweon D-G. Design and control of a nanoprecision xyΘ scanner. Rev Sci Instrum 2008; 79; 045109

[10] Maeda GJ, Sato K, Hashizume H, Shinshi T. Control of an xy nano-positioning table for a compact nano-machine tool. Jsme Int J C-Dyn Con 2006; 49; 21-27

[11] Fesperman R, Ozturk O, Hocken R, Ruben S, Tsao TC, Phipps J, Lemmons T, Brien J, Caskey G. Multi-scale alignment and positioning system–maps. Prec Eng 2012; 36; 517-37

[12] Chen KS, Trumper DL, Smith ST. Design and control for an electromagnetically driven x–y–Θ stage. Prec Eng 2002; 26; 355-69

[13] Wang R, Zhang X. A planar 3-dof nanopositioning platform with large magnification. Prec Eng 2016; 46; 221-31

[14] Mori S, Hoshino T, Obinata G, Ouchi K. Air-bearing linear actuator for highly precise tracking. IEEE T Magn 2003; 39; 812-18

[15] Parmar G, Barton K, Awtar S. Large dynamic range nanopositioning using iterative learning control. Prec Eng 2014; 38; 48-56

[16] Shinno H, Yoshioka K, Taniguchi K. A newly developed linear motor-driven aerostatic x-y planar motion table system for nano-machining. CIRP Ann-Manuf Techn 2007; 56; 369-72

[17] Teo TJ, Yang G, Chen IM. A flexure-based electromagnetic nanopositioning actuator with predictable and re-configurable open-loop positioning resolution. Prec Eng 2015; 40; 249-60

[18] Brauer JR. Magnetic Actuators and Sensors, Hoboken: John Wiley & Sons, 2006

[19] Slocum AH. Precision Machine Design. Dearborn: SME, 1992

[20] Kim WJ, Trumper DL. High-precision magnetic levitation stage for photolithography. Prec Eng 1998; 22; 66-77

[21] Liebman MK. Rotary - Linear Axes for High Speed Machining. PhD Thesis, Cambridge: Massachusetts Institute of Technology, 2001

[22] Lu XD, Trumper DL. Ultrafast tool servos for diamond turning. CIRP Ann-Manuf Techn 2005; 54; 383-88

[23] Chu CL, Fan SH. A novel long-travel piezoelectric-driven linear nanopositioning stage. Prec Eng 2006; 30; 85-95

[24] Liu YT, Higuchi T, Fung RF. A novel precision positioning table utilizing impact force of spring-mounted piezoelectric actuator, part I: experimental design and results. Prec Eng 2003; 27; 14-21

[25] Buice ES, Otten D, Yang RH, Smith ST, Hocken RJ, Trumper DL. Design evaluation of a single-axis precision controlled positioning stage. Prec Eng 2009; 33; 418-24

[26] Michellod Y, Mullhaupt P, Gillet D. Strategy for the control of a dual-stage nano-positioning system with a single metrology. In: Proceedings of IEEE Conference on Robotics, Automation and Mechatronics, Bangkok, Thailand. 2006

[27] Shinno H, Yoshioka H, Sawano H. A newly developed long range positioning table system with a sub-nanometer resolution, CIRP Ann-Manuf Techn 2011; 60; 403-06

[28] Cheng F, Fan K-C, Miao J, Li B-K, Wang H-Y. A bpnn-pid based long-stroke nanopositioning control scheme driven by ultrasonic motor. Prec Eng 2012; 36; 485-93

[29] Ghazaly MM, Sato K. Characteristic switching of a multilayer thin electrostatic actuator by a driving signal for an ultra-precision motion stage. Prec Eng 2013; 37; 107-16

[30] Okyay A, Khamesee MB, Erkorkmaz K. Design and optimization of a voice coil actuator for precision motion applications. IEEE T Magn 2015; 51; 8202811

[31] New Way Air Bearings. Air Bearing Application and Design Guide. [online] Aston: New Way Air Bearings, 2006. Available at: <http://www.newwayairbearings.com/ sites/ default/files/new_way_application_and_design_guide_%20Rev_E_2006-01-18.pdf> [Accessed 12 August 2016]

[32] Slocum A, Basaran M, Cortesi R, Hart AJ. Linear motion carriage with aerostatic bearings preloaded by inclined iron core linear electric motor. Prec Eng 2003; 27; 382-94

[33] New Way Air Bearings. Air Bushings - Metric- 20mm ID. [online], 2017. Available at: <http://www.newwayairbearings.com/products/air-bushings-metric/air-bushings-metric-20mm-id> [Accessed 27 June 2017]

[34] Sriyotha P, Nakamoto K, Sugai M, Yamazaki K. Development of 5-axis linear motor driven super-precision machine. CIRP Ann-Manuf Techn 2006; 55; 381-84

[35] Quanser. Linear Current Amplifier Module, User's Guide, Version 2.0. [pdf] Quanser, 2012

[36] The Mathworks Inc. Optimization Toolbox^{TM}, User's Guide. [online] The Mathworks Inc., 2011. Available at: < http:// www.mathworks.com/ help/ releases/ R2011b/ pdf_doc/ optim/ optim_tb.pdf > [Accessed 17 August 2016].

[37] Franklin GF, Powell JD, Emami-Naeini A. Feedback Control of Dynamic Systems, 6th ed. Upper Saddle River: Pearson, 2010

[38] Skogestad S, Postlethwaite I. Multivariable Feedback Control: Analysis and Design. Chichester: John Wiley & Sons, 1996

[39] Okyay A. Mechatronic Design, Dynamics, Controls, and Metrology of a Long-Stroke Linear Nano-Positioner. PhD Thesis, Waterloo: University of Waterloo, 2016.

[40] Dr. Johannes Heidenhain GmbH. Exposed Linear Encoders. [online] Dr. Johannes Heidenhain GmbH, 2016. Available at: < http://www.heidenhain.de/fileadmin/pdb/media/img/208960-2D_Exposed_ Linear_Encoders_01.pdf > [Accessed 18 August 2016]

[41] Monkhorst W. Dynamic Error Budgeting, A Design Approach. Graduation Thesis, Delft: University of Technology, Delft, 2004

[42] Bendat JS, Piersol AG. Random Data: Analysis and Measurement Procedures. New York: John Wiley & Sons, 1971

[43] Erkorkmaz K, Altintas Y. High speed cnc system design, part II: modeling and identification of feed drives. Int J Mach Tool Manu 2001; 41; 1487-1509

[44] Heydemann PLM. Determination and correction of quadrature fringe measurement errors in interferometers. Appl Optics 1981; 20; 3382 - 84
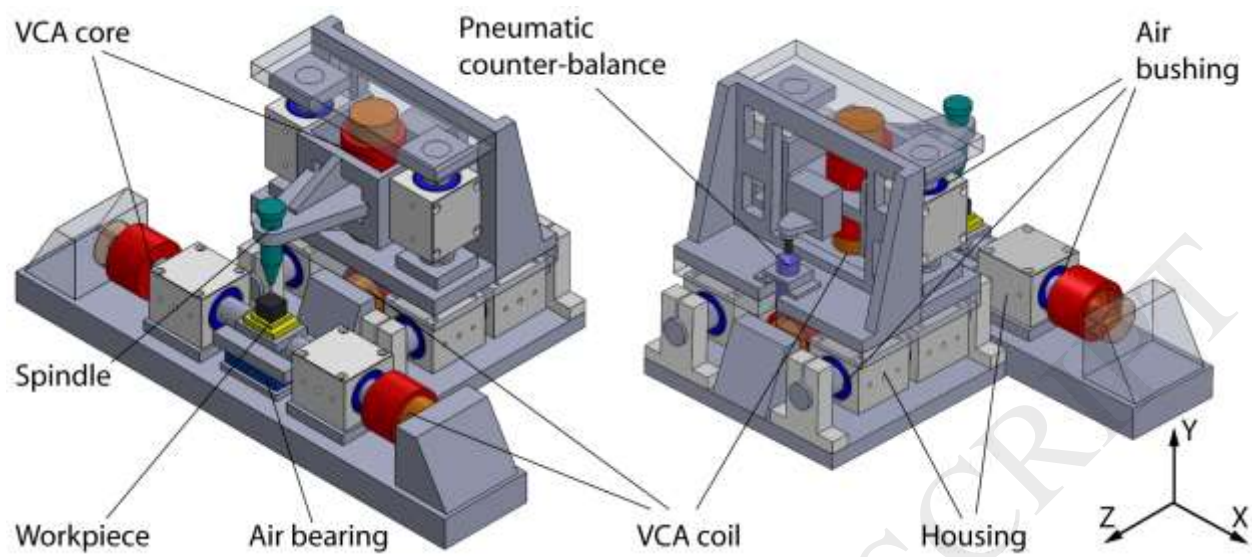
Fig. 1 Conceptual design of a low-cost desktop micro-milling machine.
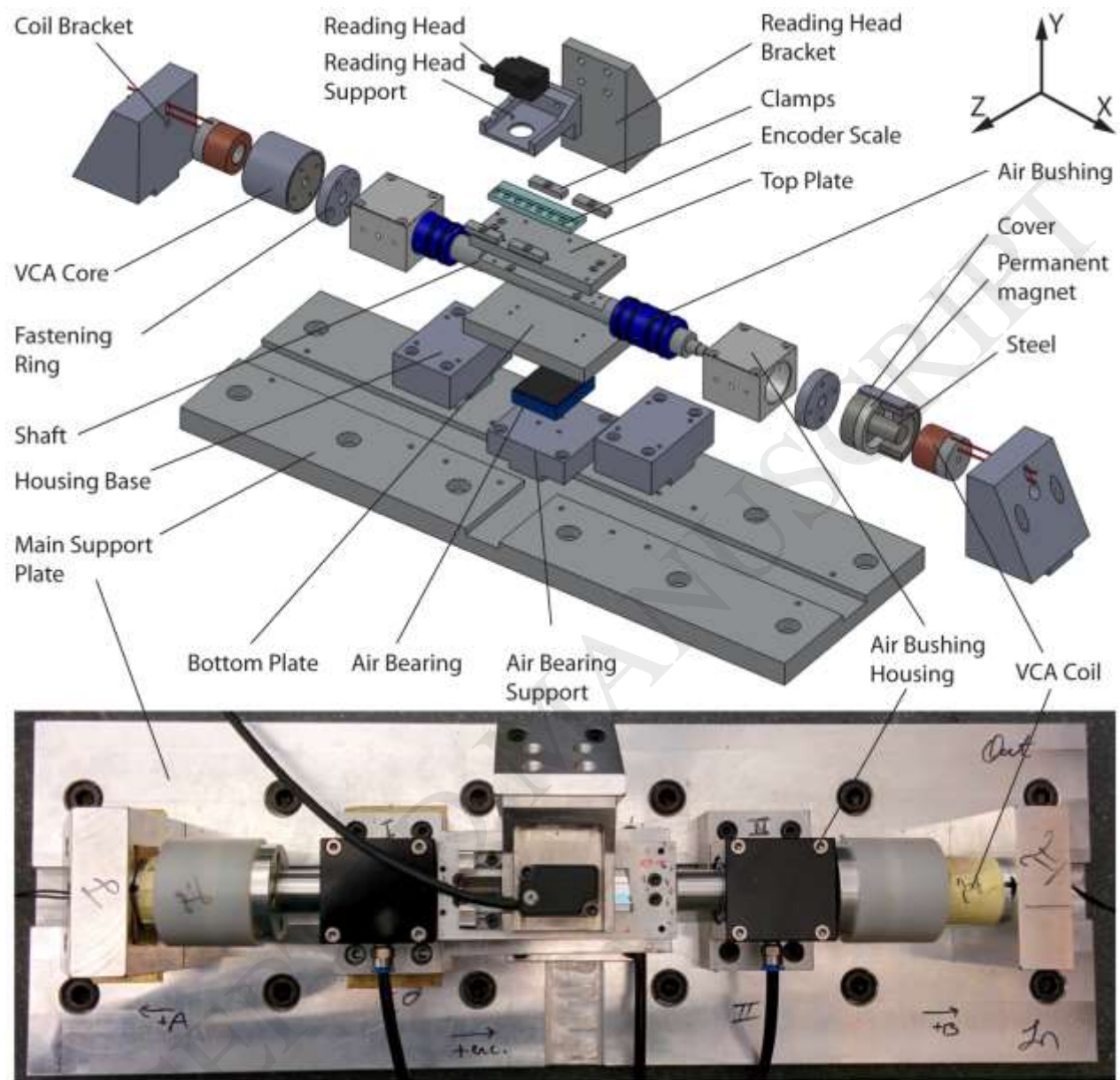
Fig. 2 Exploded view and photograph of the long-stroke linear nano-positioner.
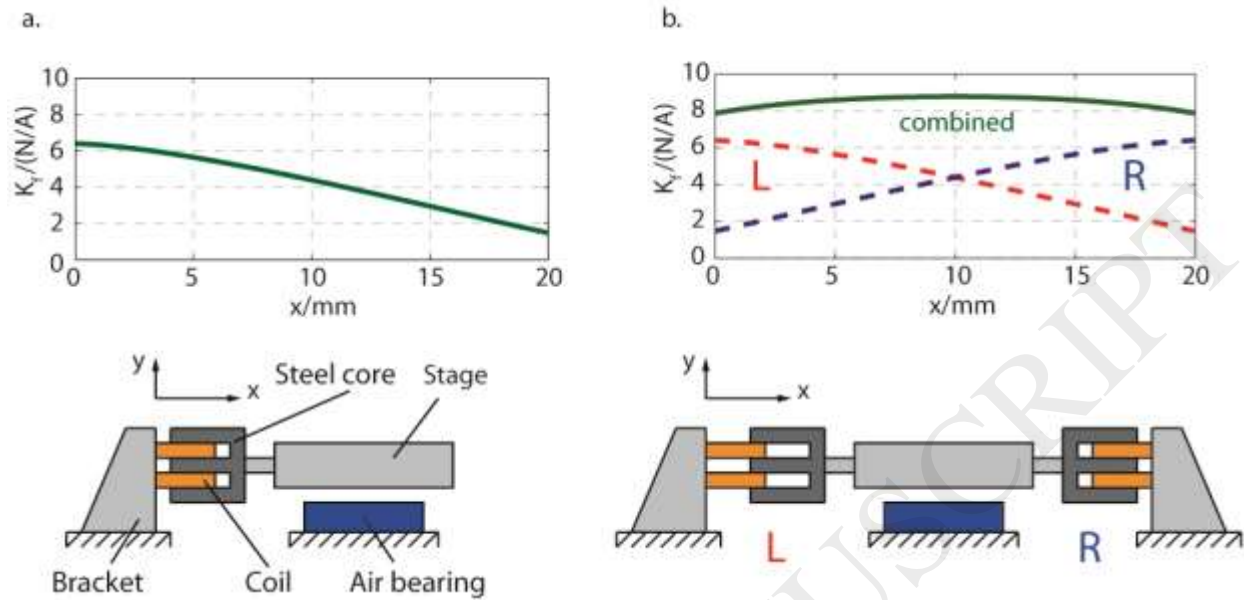
Fig. 3 Force factor vs. stroke position; a. single VCA, b. complementary double VCA.
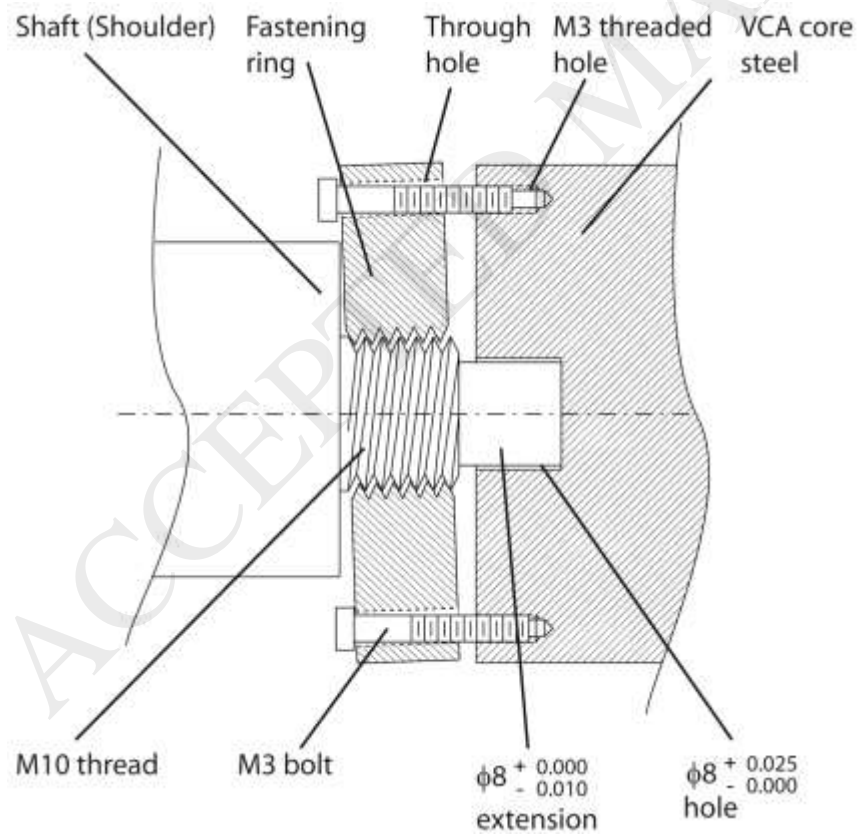
Fig. 4 VCA alignment to the shaft. Dimensions in mm.
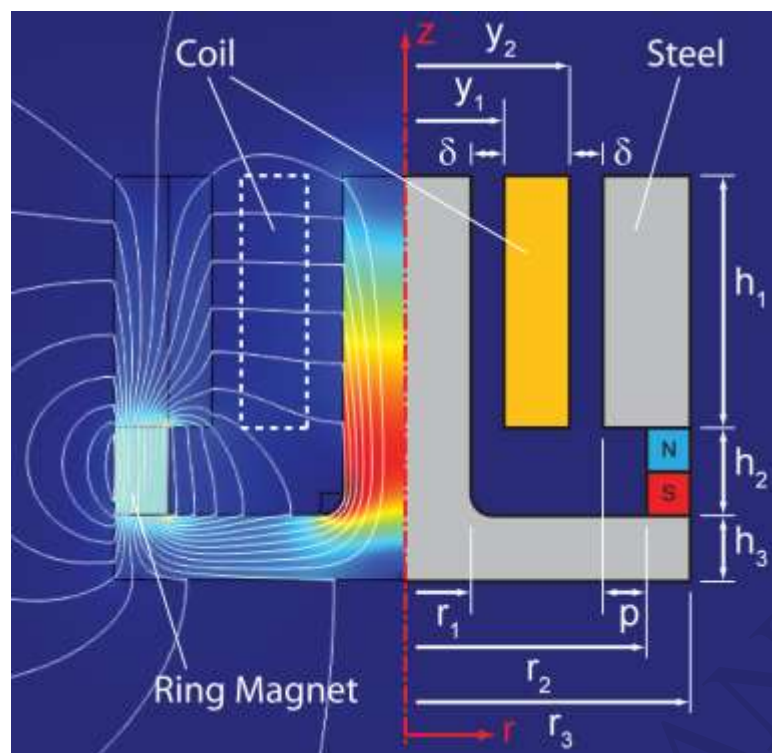
Fig. 5 Schematic drawing of the VCA.
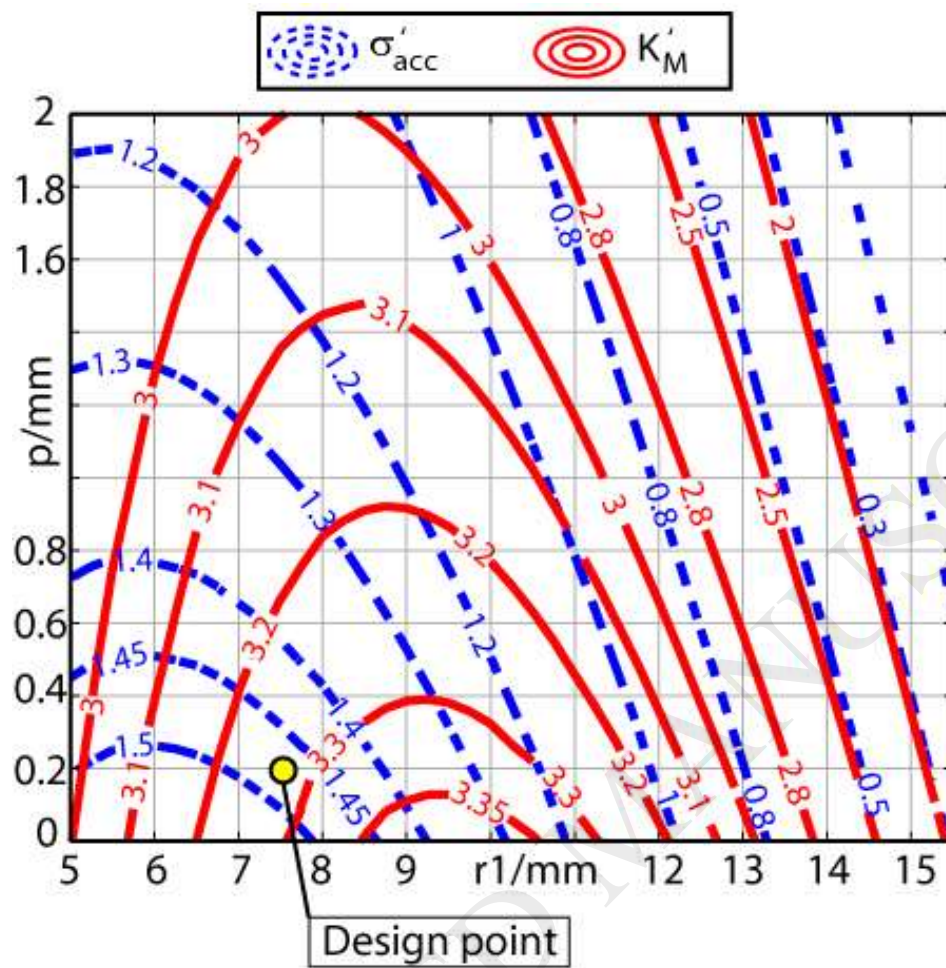
Fig. 6 Performance topologies.
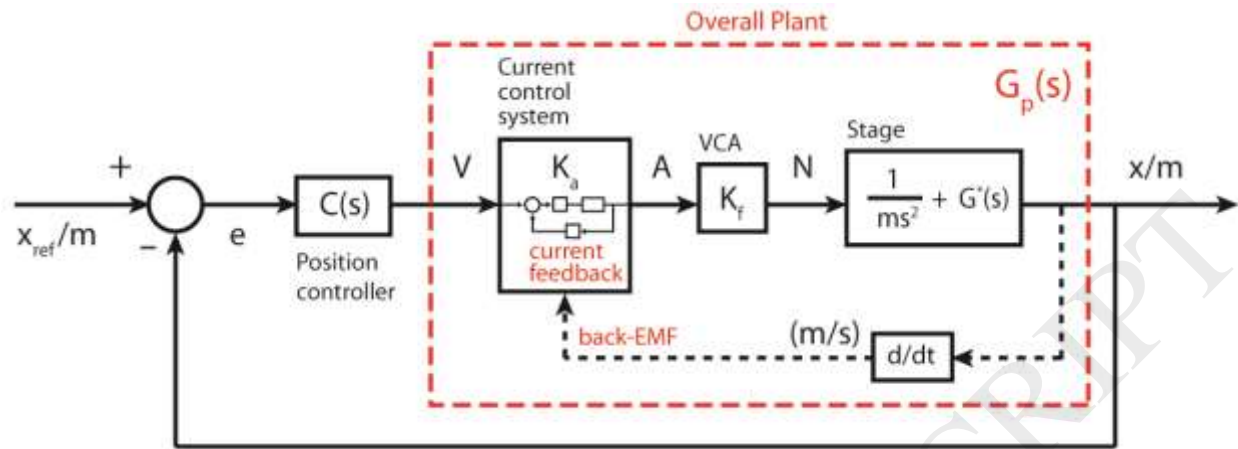
Fig. 7 Overview of the position control loop.
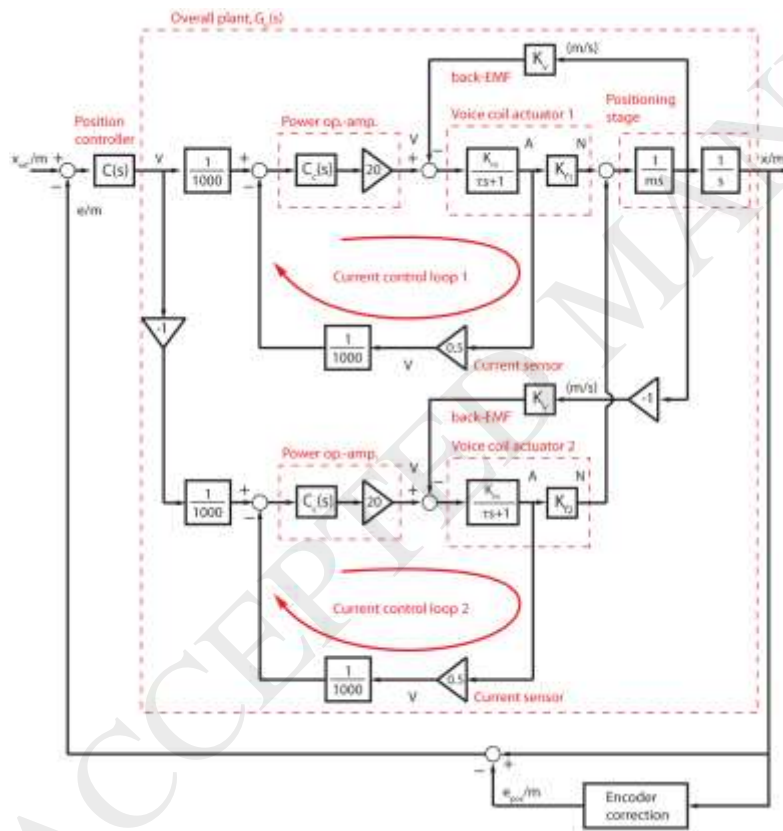
Fig. 8 Detailed control block diagram.
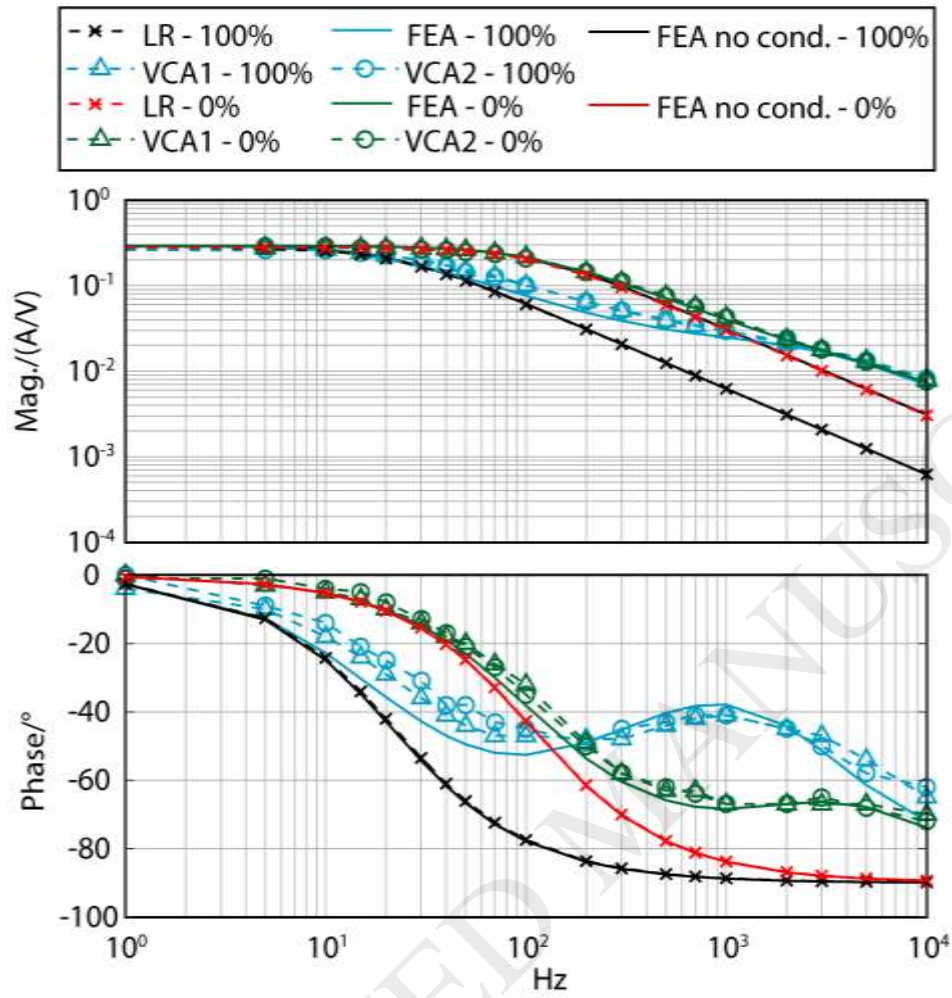
Fig. 9 Experimentally measured, FEA predicted, and first-order theoretical (LR) VCA electrical dynamics ($G_m(s)$).

24
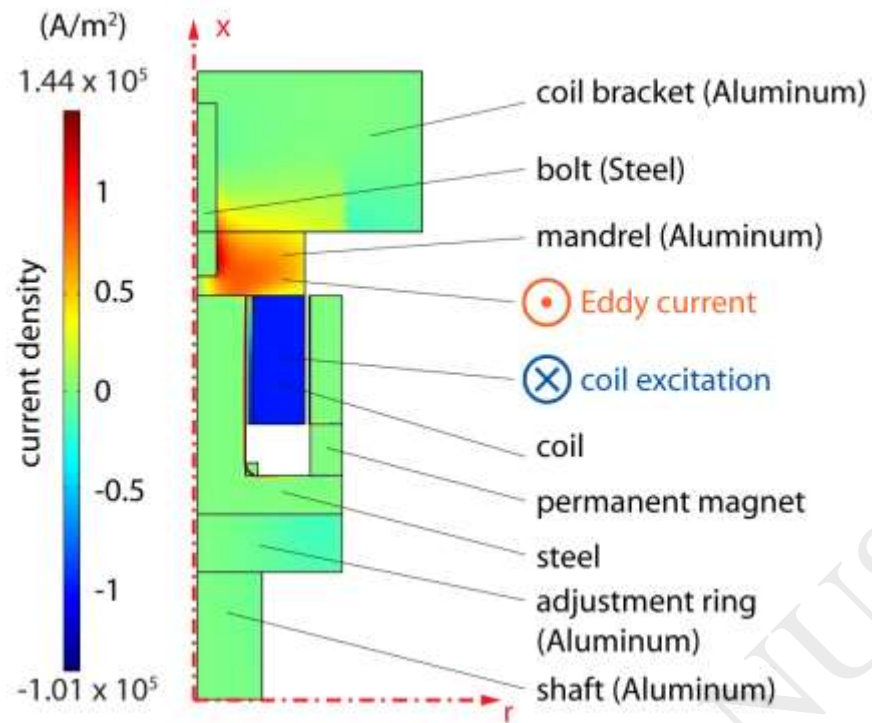
Fig. 10 Current FRF simulation using FEA for the fully engaged VCA at 200 Hz.
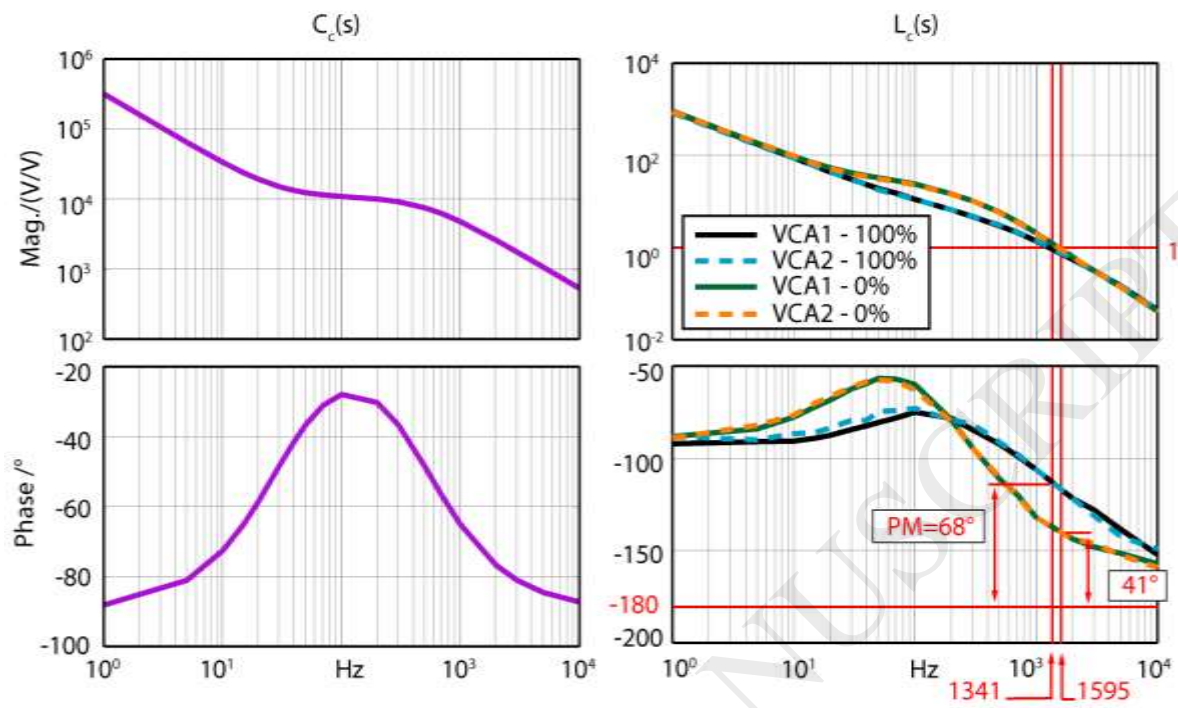
Fig. 11 Controller (C_c) and loop (L_c) transfer functions.
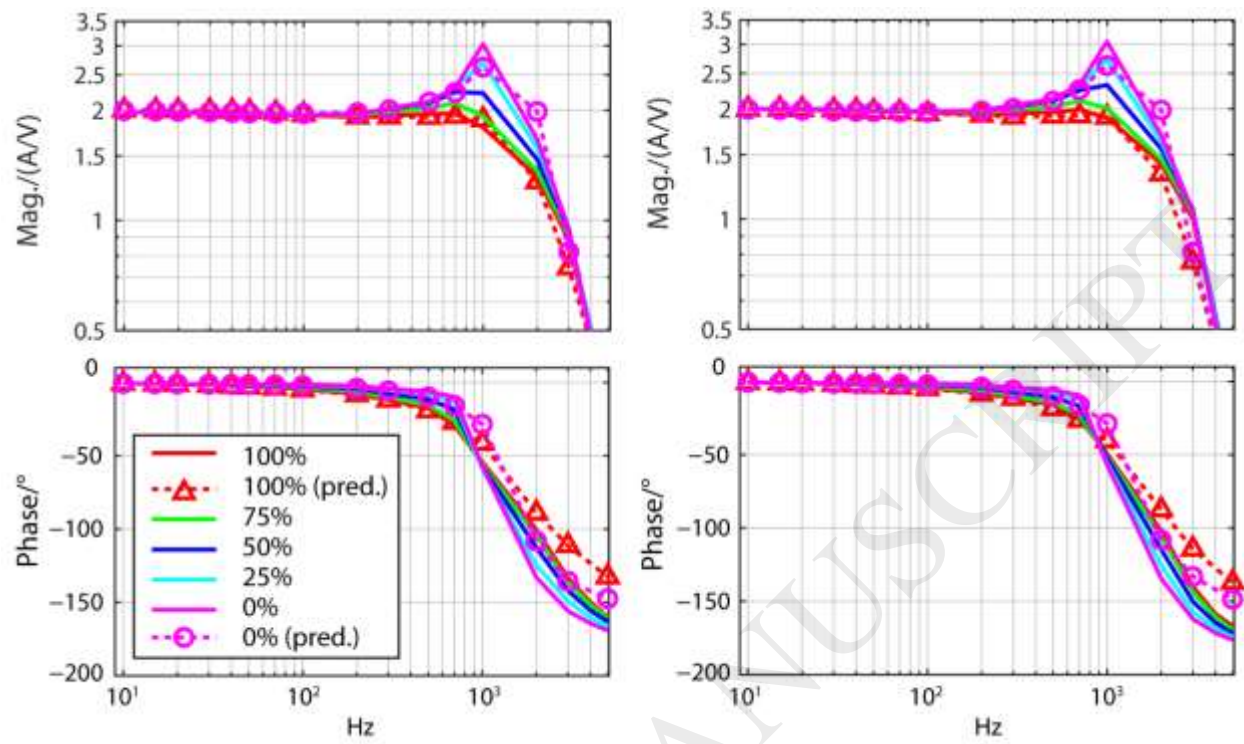
Fig. 12 Current control CLTF.
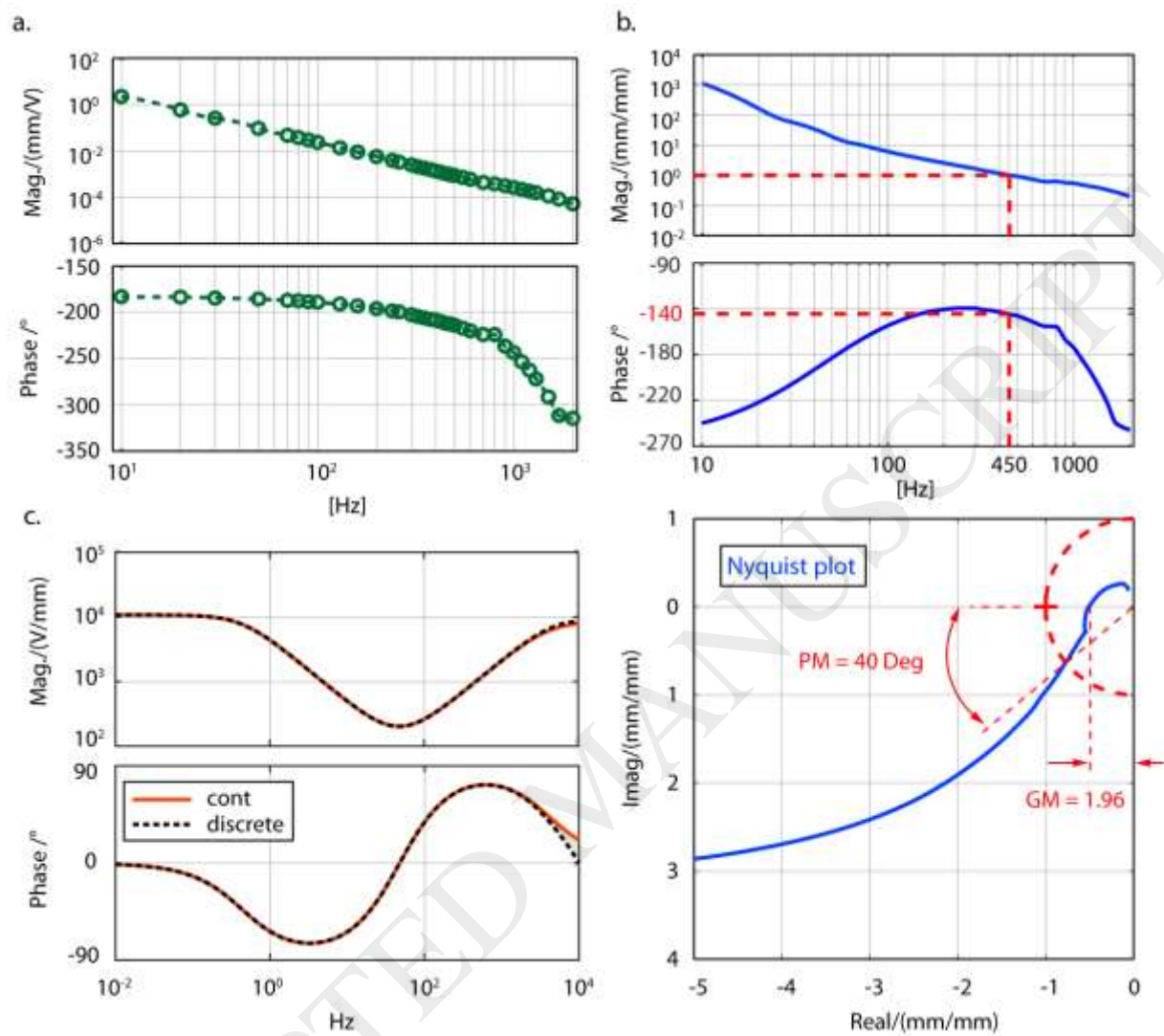
Fig. 13 Transfer functions related to the position controller design; a. Measured $G_p(s)$, b. Positioning loop TF ($L(s)$), c. Position controller ($C(s)$).
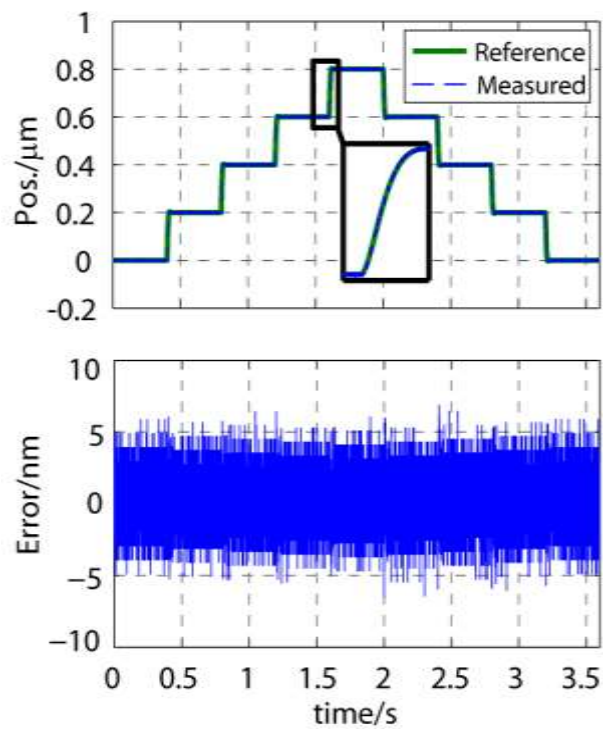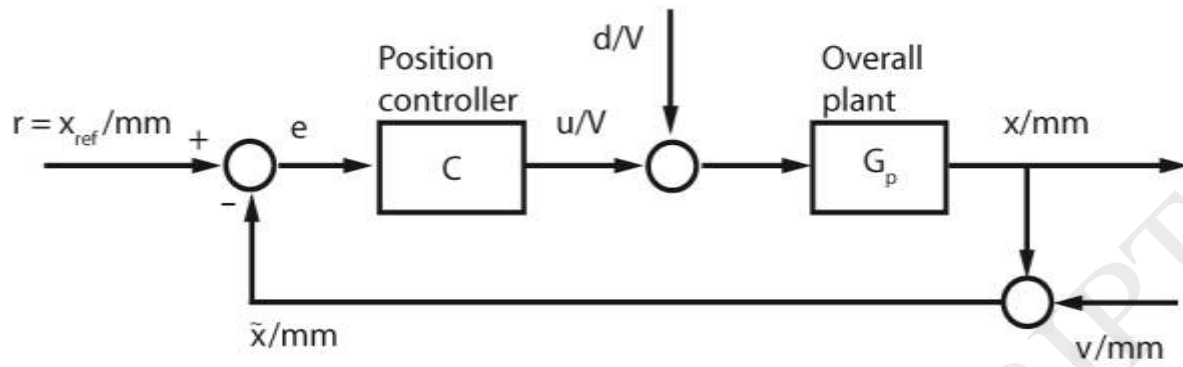
Fig. 14 Positioning results with the step trajectory.

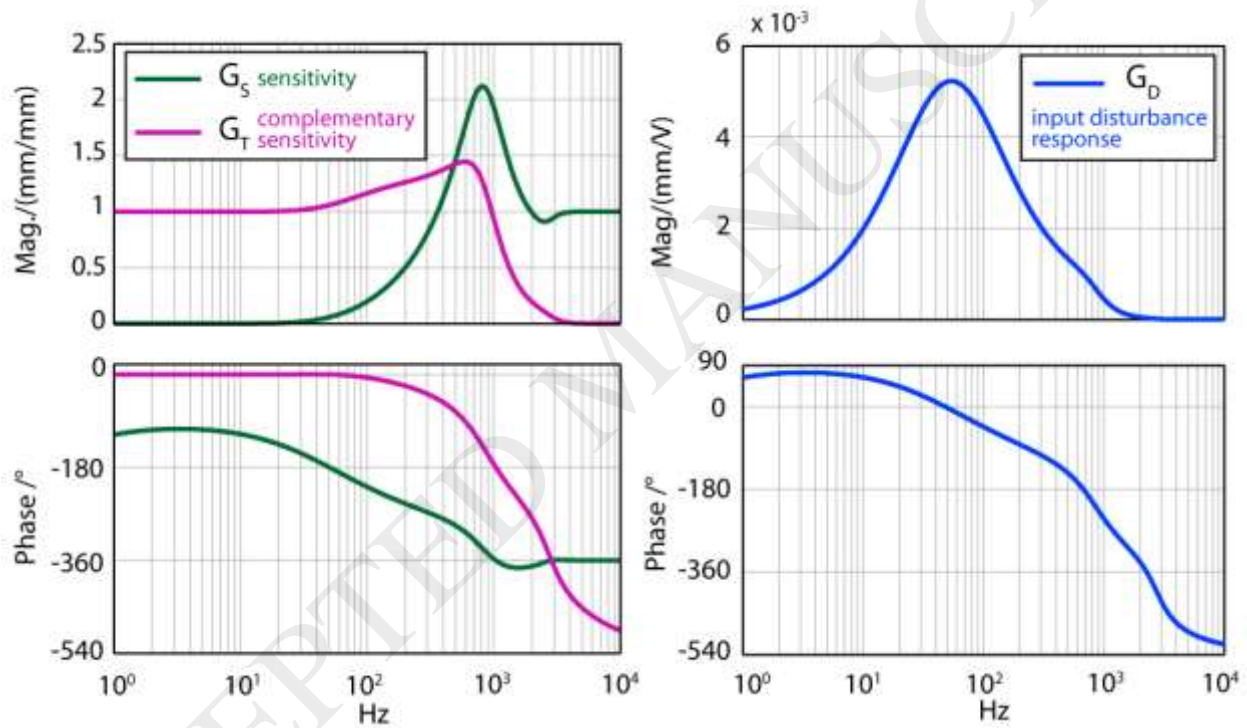Fig. 15 Block diagram with the disturbance and measurement noise signals.

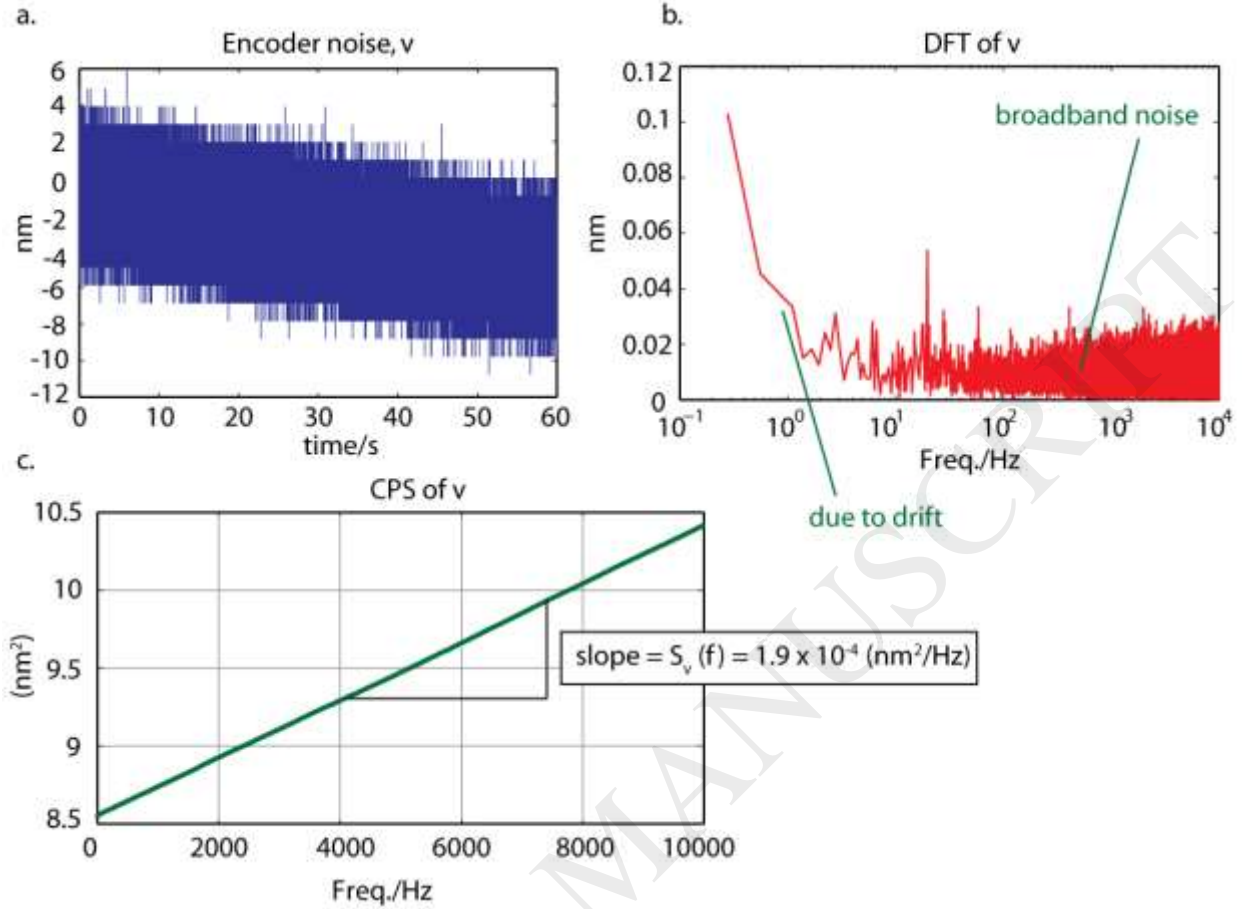Fig. 16 Bode plots of transfer functions used in DEB analysis.

30

Fig. 17 Determination of the encoder noise PSD ($S_v(f)$); a. Time domain signal measured at a static position, b. DFT of v, c. CPS of v.
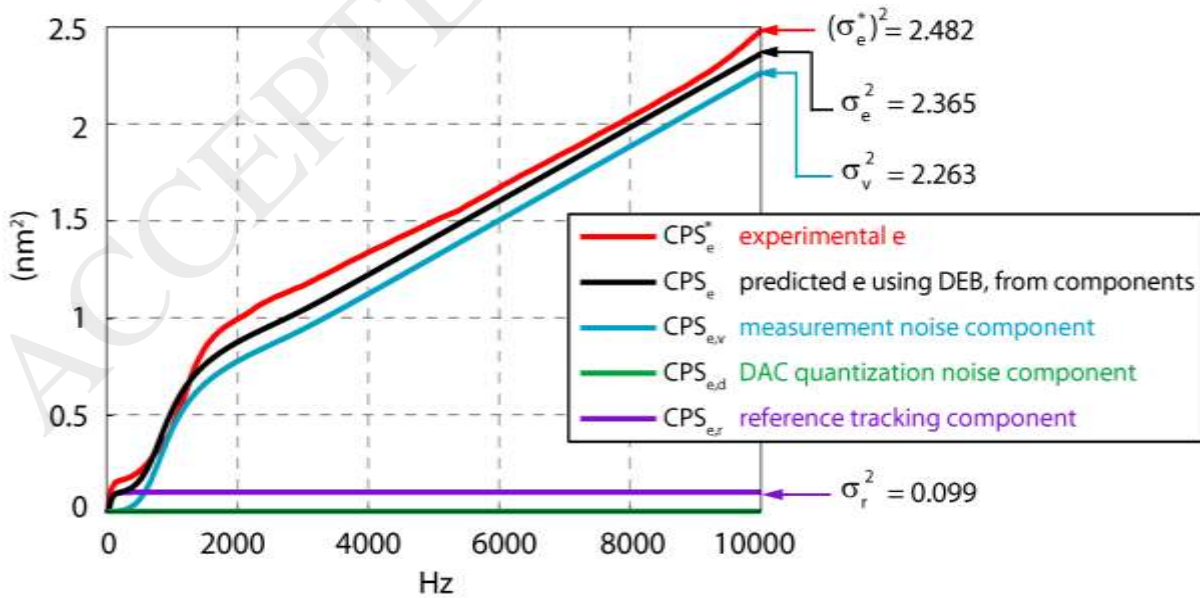

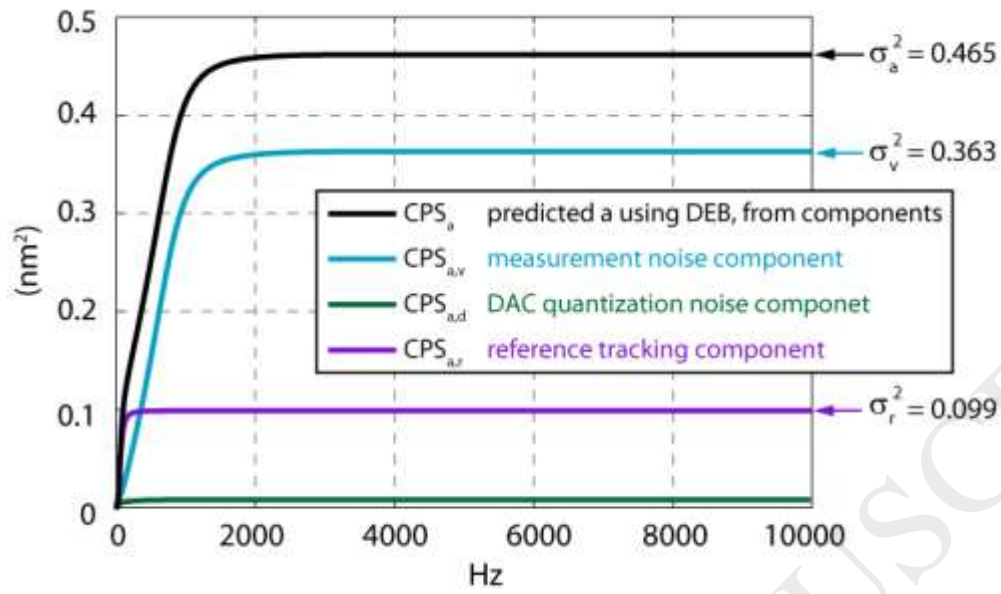Fig. 18 Cumulative power spectrum of the control error (e).

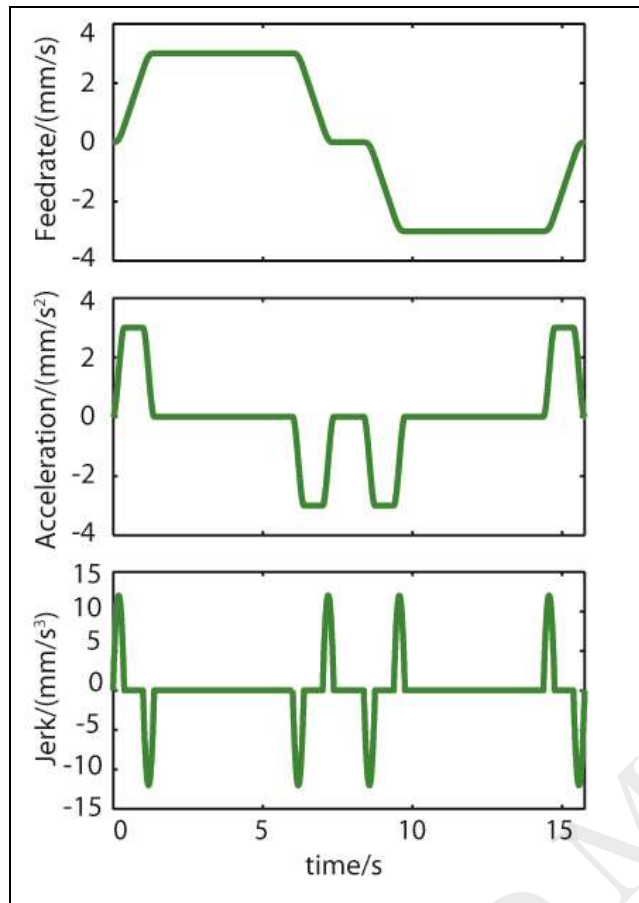Fig. 19 Cumulative power spectrum of the actual positioning error.

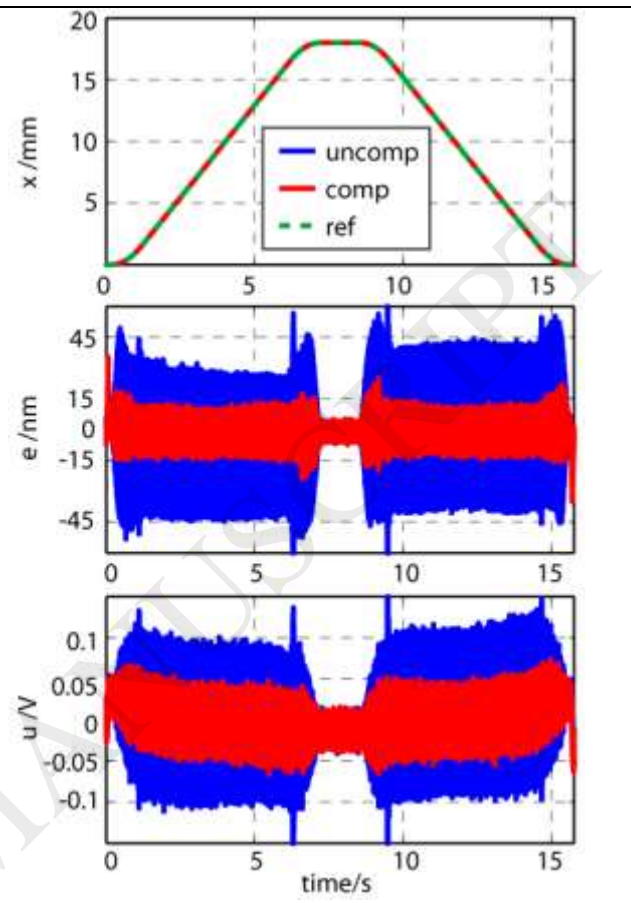Fig. 20 Jerk limited cubic acceleration profile trajectory.

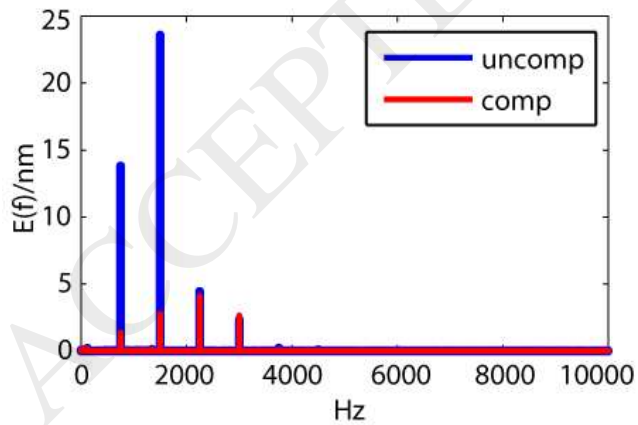Fig. 21 Trajectory tracking results.

Fig. 22 DFT of the control error.

Table 1. VCA design variables.

Symbol	Description	Value/mm	Symbol	Description	Value/mm
h_1	stroke length	20	r_3	magnet outer radius	22.5
h_2	magnet height	8	p	reduction in gap	0.2
h_3	core base height	6	δ	clearance	0.5
r_1	core inner radius	7.5	y_1	coil inner radius	$r_1 + \delta$
r_2	magnet inner radius	17.5	y_2	coil outer radius	$r_2 - p - \delta$

Table 2. Pole/zero/gain fitted to the current response.

engagement	p_1/Hz	$(1/\tau)$/Hz	p_2/Hz	p_3/Hz	z_1/Hz	z_2/Hz	K
100%	21	22	146	3010	84	434	452
0%	103	109	375	5494	287	2611	518

Table 3. Current control cross-over frequencies and phase margins.

	VCA 1 - 100%	VCA 2 - 100%	VCA 1 - 0%	VCA 2 - 0%
Cross-over freq., ω_c /Hz	1341	1375	1595	1592
Phase margin, PM/°	68	68	41	41

Table 4. Current control bandwidths.

	VCA	BW/Hz	Phase/°	Engagement
Best	1	1804	-94	100%
(at -3 dB)	2	1990	-102	100%
Worst	1	907	-44	0%
(at +3 dB)	2	915	-45	0%

Table 5. Definitions of terms used in DEB calculations.

Symbol	Definition	Expression
T_s	Sampling time	1/20000 s
df	Frequency grid	-
f	Frequency array	$f_k = \sum_{i=1}^{k} df$, $1<k<N$ $f_N = 1/2T_s$ (Nyquist frequency)
$W(f)$	Discrete Fourier transform	Matlab® 'fft' function is used on the time domain signal.
$S(f)$	One-sided power spectral density (PSD)	$S(f) = \dfrac{2 \cdot \left| W(f) \right|^2}{df}$
$CPS(f)$	One-sided cumulative power spectrum	$CPS\left(f_k\right) = \sum_{i=1}^{k} S_i\, df$, $1<k<N$
σ^2	Variance	*from the time domain signal:* Matlab® 'var' function is used. *from the spectrum:* $\sigma^2 = CPS\left(f_N\right)$
σ	Standard deviation (equals to root-mean-square (RMS) if the signal has zero mean)	$\sqrt{\sigma^2}$

Table 6. Parameters of the distorted signal model.

a /V	0.4741
b /V	0.4492
A_o /V	0.0011
B_o /V	0.0052
θ /°	-0.2320

Table 7. DFT of control error.

E (f)/nm		Freq./Hz
Uncompensated	Compensated	
13.81	1.38	750
23.57	2.78	1500
4.45	4.09	2250
2.35	2.66	3000